

Magnetic imaging with an ensemble of Nitrogen Vacancy centers in diamond.

M. Chipaux¹, A. Tallaire², J. Achard², S. Pezzagna³, J. Meijer³, V. Jacques⁴, J.-F. Roch⁴, and T. Debuisschert^{1*}

¹ *Thales Research and Technology, 1 av. Augustin Fresnel, F-91767 Palaiseau CEDEX, France*

² *Laboratoire des Sciences des Procédés et des Matériaux, CNRS and Université Paris 13, 93340 Villetaneuse, France*

³ *Institut für Experimentelle Physik II, University Leipzig, Leipzig, Germany and*

⁴ *Laboratoire Aimé Cotton, CNRS, Université Paris-Sud and Ecole Normale Supérieure de Cachan, 91405 Orsay, France*

The nitrogen-vacancy (NV) color center in diamond is an atom-like system in the solid-state which specific spin properties can be efficiently used as a sensitive magnetic sensor. An external magnetic field induces Zeeman shifts of the NV center levels which can be measured using Optically Detected Magnetic Resonance (ODMR). In this work, we exploit the ODMR signal of an ensemble of NV centers in order to quantitatively map the vectorial structure of a magnetic field produced by a sample close to the surface of a CVD diamond hosting a thin layer of NV centers. The reconstruction of the magnetic field is based on a maximum-likelihood technique which exploits the response of the four intrinsic orientations of the NV center inside the diamond lattice. The sensitivity associated to a $1 \mu\text{m}^2$ area of the doped layer, equivalent to a sensor consisting of approximately 10^4 NV centers, is of the order of $2 \mu\text{T}/\sqrt{Hz}$. The spatial resolution of the imaging device is 400 nm, limited by the numerical aperture of the optical microscope which is used to collect the photoluminescence of the NV layer. The versatility of the sensor is illustrated by the accurate reconstruction of the magnetic field created by a DC current inside a copper wire deposited on the diamond sample.

INTRODUCTION

Measuring a magnetic field is a generic tool to investigate physical effects involving charge or spin displacement that appear in various fields such as spintronics, nanoelectronics, life-science. Examples are spin currents in graphene or carbone nanotubes, current propagation in nanoelectronics circuits, neuronal activity inducing a displacement of the action potential. In addition to sensitivity and spatial resolution, measuring not only the field intensity but also the full vectorial components is particularly valuable, as well as the ability to produce a full image of the sample.

During the past few decades a wealth of methods has been developed to sense and image magnetic fields. Various detection techniques using superconducting quantum interference devices (SQUID) [1], magnetic resonance force microscopy (MRFM)[2, 3], alkali vapour atomic magnetometers [4, 5], and Bose-Einstein condensates (BEC) have been investigated.

A particularly attractive technique is to develop magnetometers based on Nitrogen Vacancy centers (NV) inserted in ultrapure diamond. The NV center is a point defect in diamond. It consists of a substitutional nitrogen atom (N) associated with a vacancy (V) located in an adjacent lattice site of the diamond matrix (Fig. 1 a)). It behaves as a color center that allows for optical detection of the magnetic field [6].

NV centers have numerous advantages. They can be produced as single defects with well controlled position within the diamond crystal through ion implantation. In particular, the depth of the NV centers with respect to the surface can be controlled with a precision of a few nanometers. The NV center is "trapped" in the

crystal and it can be reliably addressed and re-found. NV centers can be optically controlled and they are perfectly photostable. They are pumped in the visible light (532 nm) and emit a fluorescence signal in the near infrared (600 – 800 nm) that can be easily detected with standard optical systems.

NV centers can exhibit different charge states. The negatively charged NV center (NV^-) is a two electrons system with well defined energy levels associated with the spin state (Fig. 1 b)). An essential feature of the NV^- defect is that its ground level is a spin triplet $S = 1$, which degeneracy is lifted into a singlet state $m_S = 0$ and a doublet state $m_S = \pm 1$, separated by $\nu_0 = 2.88$ GHz in the absence of magnetic field [7]. In addition, the ground-state electron spin properties exhibit a long coherence time [8–10]. Radiative transition selection rules associated with the spin state quantum number lead to a polarization of the NV^- defect in the ground state spin level $m_S = 0$ by optical pumping (Fig. 1 b)). Furthermore, the NV defect photoluminescence intensity is significantly higher when the $m_S = 0$ state is predominantly populated [7]. Such a property allows to optically detect the spin state of a single NV center by Optically Detected Magnetic Resonance (ODMR). Indeed, applying a microwave field at 2.88 GHz on single NV^- center, initially prepared in the $m_S = 0$ state through optical pumping drives it to the $m_S = \pm 1$ spin state and results in the observation of a dip in photoluminescence signal. When an external magnetic field is applied, the levels corresponding to $m_S = +1$ and $m_S = -1$ are shifted due to Zeeman effect and their resonance frequencies denoted ν^+ et ν^- are shifted accordingly (Fig. 1 c)). For magnetic fields lower than a few hundreds of Gauss [11], the Zeeman effect is linear and the positions of the lines are

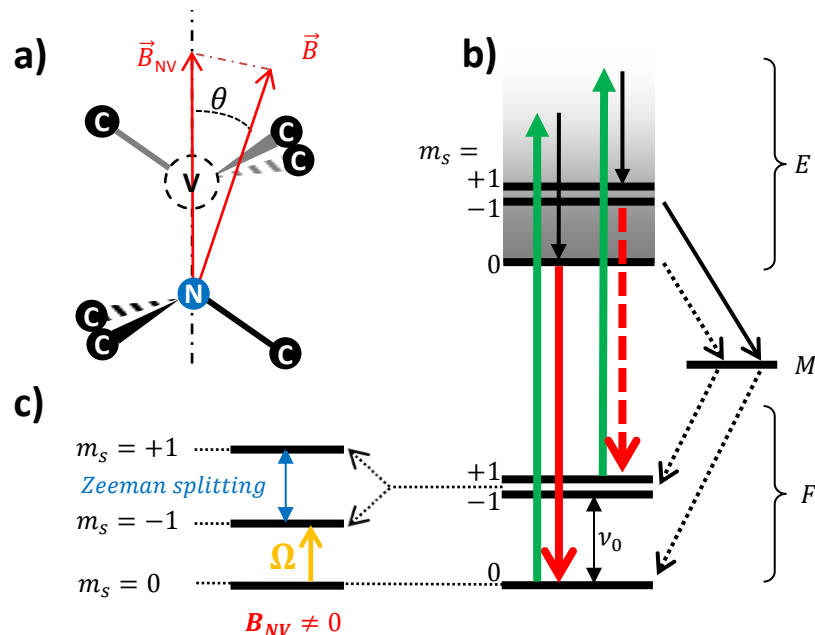


FIG. 1: **a)** Structure of the NV center. A Nitrogen atom (N), substituted to a Carbon (C) in the diamond lattice, is coupled to a Vacancy (V) located on an adjacent crystallographic site. The NV center is sensitive to the projection \vec{B}_{NV} of the magnetic field \vec{B} on the N-V axis. The NV^- color centre is a two electrons system which electronic diagram is depicted in **b)**. It is formed by two spin triplet states denoted F (Fundamental) and E (Excited) and one singlet metastable state M. In the absence of magnetic field, spin states $m_S = +1$ and $m_S = -1$ are lifted from state $m_S = 0$ due to spin-spin interaction. The corresponding frequency transition is $\nu_0 = 2.88$ GHz in the fundamental spin triplet. Spin conserving optical transitions can occur between the levels and are represented in green (absorption) and red (emission). Non radiative transitions are represented in black. The $m_S = +1$ and $m_S = -1$ levels are more strongly coupled to the metastable level (solid arrow) than the $m_S = 0$ level is (dashed arrow). This dissymmetry explains, first, the possibility to polarize the NV^- center in the $m_S = 0$ spin state by optical pumping in the visible (e.g. $\lambda_p = 532$ nm), and, second, the higher rate of photoluminescence when the NV center is in spin state $m_S = 0$ than when it is in states $m_S = +1$ and $m_S = -1$. **c)** In the presence of a magnetic field \vec{B} , the degeneracy between state $m_S = +1$ and $m_S = -1$ is lifted proportionally to the field projection on the N-V axis. Those magnetic resonances can be detected applying a microwave field that induces transitions between the states $m_S = 0$ and the states $m_S = +1$ or $m_S = -1$ when its frequency Ω is resonant with the transition frequency. A consecutive decrease of the photoluminescence allows to optically detect the resonance (ODMR).

given by:

$$\nu^\pm - \nu_0 = \pm \frac{g\mu_b}{h} \cdot B_{NV} \quad (1)$$

where $\nu_0 = 2.88$ GHz is the zero field splitting of the ground state, and $\frac{g\mu_b}{h} = 28$ MHz/mT is the electron spin gyromagnetic ratio. The distance between the two lines $D\nu = \nu^+ - \nu^-$ scales linearly with the projection of the magnetic field along the (N-V) axis, B_{NV} , with the factor:

$$\frac{D\nu}{B_{NV}} = 56 \text{ MHz/mT} \quad (2)$$

Due to the C_{3v} symmetry of the NV center, four axes orientations are possible, leading to four different possible projections of the magnetic field. Therefore, the ODMR spectrum of an ensemble of NV^- centers exhibits four pairs of lines that can be exploited for vectorial reconstruction of the applied magnetic field.

The unique properties of NV^- centers can lead to solid-state, room temperature, optically addressed magnetic sensors [12] in a wide range of emerging technologies, from imaging in life science [13], to high-resolution magnetic sensing [14, 15] and digital quantum processing [16–18].

Two main kinds of NV based magnetometers have been developed up to now. Scanning probe magnetometers make use of a monolithic all-diamond scanning probe tip containing a single NV centre within ~ 10 nm from its end [19]. Sensitivity of ~ 300 nT/ \sqrt{Hz} [20, 21] and spatial resolution of ~ 10 nm can be obtained [20]. An alternative solution consists in fixing a nanodiamond containing a single NV at the end of an Atomic Force Microscope tip [22]. Such technique has been used recently to visualize domain walls displacement between ferroelectric domains [23].

The alternative solution is to use a high-density en-

semble of NV centres. Collecting the signal from an ensemble of N NV centers should result in a signal to noise enhancement in \sqrt{N} with respect to a single NV center. Several devices exploiting that property have been demonstrated [24–26]. They make use of an active layer of NV centers located close to the surface of a bulk diamond plate. The magnetic object is located close to this surface, and the magnetic field modifies the luminescence emitted by the NV centers. A microscope objective forms a diffraction limited image of the luminescence on a camera. This gives rise to a complete data acquisition over the whole object in one shot.

In the present paper, we describe the realization of such a magnetic imaging device including, first, the experimental set-up, then the data acquisition and their treatment, the magnetic field reconstruction technique and finally the evaluation of the device sensitivity.

EXPERIMENTAL SET-UP

The central element of the sensor is the diamond slab, holding a thin layer of NV centers implanted close to the surface, represented on Fig. 2. It is obtained from a (100) oriented diamond sample grown by plasma assisted Chemical Vapour Deposition (CVD) [27] on an High Pressure High Temperature (HPHT) substrate. The ultra-pure, single domain, 600 μm thick sample is then cut to produce a 3 mm side, 250 μm thick slab. This thickness is chosen to allow the collection of the luminescence of the NV layer located on the back face through the diamond slab, taking into account the working distance of the microscope objective $WD = 320 \mu\text{m}$. This makes possible the study of opaque magnetic samples positioned underneath the slab (Fig. 2). Moreover, this thickness ensures good mechanical stability thus allowing optical quality polishing of the two main faces, which results in good imaging quality. In addition, the four lateral faces are also optically polished to allow side pumping.

In order to produce the suitable NV^- layer, the diamond is uniformly implanted [28] with $^{15}\text{N}^{2+}$ ions at the density of 10^{14} N/cm^2 , at the limit of diamond graphitization. This concentration allows a high density of NV centres while avoiding luminescence quenching by neighboring Nitrogen atoms. The implantation energy is 5 keV, which results in a layer located at about $8 \pm 2 \text{ nm}$ below the surface. Thus, the distance between the NV^- layer and the magnetic sample located close to the surface may be very small in order to obtain good spatial resolution. With this energy, around 1 % of the $^{15}\text{N}^{2+}$ ions are converted in NV^- centres, which results in a surface concentration around $10^4 \text{ NV}/\mu\text{m}^2$. The Nitrogen atom has a nuclear spin that induces a hyperfine structure that is not resolved in our measured spectra, and thus contributes to the OMDR lines broadening. Choosing the ^{15}N isotope (nuclear spin 1/2) results in a two

line hyperfine structure and a slightly smaller broadening than in the case of the natural ^{14}N isotope with nuclear spin 1 and a three lines hyperfine structure. In addition, the specific hyperfine structure is a signature of the implanted ^{15}N isotope that is not present naturally as an impurity in diamond.

Two configurations have been considered in order to optically pump the NV^- layer. The first one, not represented here, consists in focusing the pump beam in the image principal plane of the microscope objective [24, 25] in order to obtain a collimated beam on the object side. However, after having pumped the NV^- layer, the beam can heat the sample and may damage it depending on its power. We have implemented an alternative solution [26], represented in Fig. 2 a), that consists in propagating the pump beam into the diamond sample thanks to total internal reflections on the main faces, taking benefit of the high index of diamond $n_{\text{dia}} = 2.4$. To achieve that, the pump beam is incident on one side face of the diamond slab, and then experiences zigzag propagation until it reaches the active layer located in the field of view of the microscope objective. In our set-up, the pump laser is a Coherent - Verdi V5 producing a $P_{\text{pump}} = 150 \text{ mW}$ power beam at $\lambda_{\text{pump}} = 532 \text{ nm}$.

The photoluminescence from the NV^- layer is collected with an immersion microscope objective having a high numerical aperture ($\text{N.A} = 1.35$). This results in a 8.7 % collection efficiency and a diffraction limited resolution of 400 nm. The magnification of the microscope can be chosen by proper selection of its focusing lens. The NV^- layer is imaged on the focal plane of an IDS camera with E2V CMOS sensor. The main characteristics of the imaging system such as pixel size of the camera, typical magnification value and the corresponding pixel sizes on the sample are given in Table I.

For a typical exposure time of $T = 2.5 \text{ ms}$ and a signal to noise ratio $\frac{S}{N}$ close to 100, a pixel returns a signal close to saturation. Those values are consistent with the sensitivity of the camera which shows that the number of photons required to obtain a signal close to saturation corresponds to the signal to noise ratio $\frac{S}{N} = 100$ we have measured. In addition, we have measured that the signal to noise evolves as \sqrt{S} , which is the signature of shot-noise.

Finally, an omega shape antenna formed by a short-circuit at the end of a coaxial cable powered by a frequency tunable microwave synthesizer provides an oscillating microwave magnetic field that is used to induce the magnetic resonances of the NV centres. The antenna shape has been chosen in order to provide a uniform microwave magnetic field over the field of view of the microscope objective.

The main characteristics of the experimental set-up are collected in Table I.

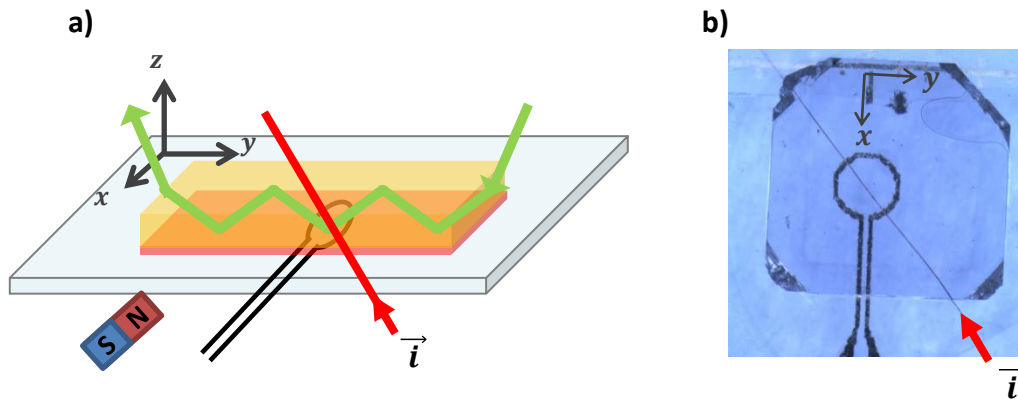


FIG. 2: **a)** - Scheme of the experiment. The CVD diamond slab (yellow) is implanted with a thin layer of nitrogen vacancy centers close to the surface (transparent red). The pump beam is incident on an optically polished side of the slab and it experiences total internal reflections on the main faces until it reaches the area located close to the sample. The luminescence is emitted by the NV centers in the z direction. For the sake of clarity, we have not represented the microscope objective that collects the luminescence towards the CMOS camera. The diamond slab is positioned above a glass plate holding a lithographed short-circuit omega shape antenna allowing to apply the microwave excitation. The $20\ \mu\text{m}$ diameter copper wire holding the DC current is placed between the glass plate and the diamond slab, in contact with the implanted surface. A permanent magnet applies a static magnetic field allowing to lift the degeneracy between the four possible NV centers orientations ; **b)** - picture showing the diamond slab with the antenna and the wire holding the current.

TABLE I: Main characteristics of the pump beam, the imaging system and the measured ODMR lines.

| Parameter | symbol | value |
|-----------------------------------|------------------|--------------------|
| Pumping wavelength | λ_{pump} | 532 nm |
| Pumping power | P_{pump} | 150 mW |
| Exposure time | T | 2.5 ms |
| Size of the CMOS array pixels | e' | $5.3\ \mu\text{m}$ |
| Microscope magnification | G | 25 |
| Pixel size on the active layer | e'/G | 210 nm |
| Signal to noise ratio (one pixel) | S/N | 105 |
| Contrast of ODMR lines | C | 0.9 % |
| Linewidth (at half maximum) | $\Delta\nu$ | 6.8 MHz |

DATA ACQUISITION AND TREATMENT

The set-up described above allows to perform an image of the NV^- layer, and for each pixel, to retrieve the ODMR spectrum. The frequency of the microwave synthesizer is swept around the central frequency $\nu_0 = 2.88\ \text{GHz}$. For each frequency step, a complete luminescence image is taken (Fig. 3 a)). The images are appended in the computer memory to form a 3D volume of data giving the value of the luminescence for each pixel (x,y) of the camera and for each frequency (ν) of the sweep. This volume of data can also be considered as an image in which each (x,y) pixel returns a full ODMR spectrum. Fig. 3 b) presents such a spectrum taken from a pixel at the centre of the image. A static magnetic field is applied to shift the lines away from degeneracy. The spectrum exhibits four pairs of lines, denoted (a), (b), (c)

and (d) corresponding to the four possible orientations of the NV^- centre. Each pair (i) corresponds to the frequencies ν_i^+ and ν_i^- located symmetrically each side of the central frequency ν_0 . The distance between the two peaks in one pair is directly related to the projection B_i of the applied magnetic field on the corresponding N-V axis (Eq. 2).

The precise position of the eight resonances are determined for each pixel using the Levenberg-Marquardt algorithm [29, 30] to fit the following multi-Lorentzian, multi-parameter function on the data:

$$f(\nu) = y_0 \times \left(1 - \sum_{i=a,b,c,d} C_i \cdot \left[L\left(\frac{\nu - \bar{\nu}_i - D\nu_i/2}{\Delta\nu_i}\right) + L\left(\frac{\nu - \bar{\nu}_i + D\nu_i/2}{\Delta\nu_i}\right) \right] \right) \quad (3)$$

where $L(x) = \frac{1}{1+x^2}$ is the Lorentzian function, C_i is the contrast of the line's pair (i) , $\bar{\nu}_i = \frac{\nu_i^- + \nu_i^+}{2}$ is the central position of the pair, $D\nu_i = |\nu_i^+ - \nu_i^-|$ is the Zeeman distance between the two lines of the pair and $\Delta\nu_i$ is their linewidth.

The algorithm requires inputs for the fitting parameters that are not too far from the result. So, a pre-selection of those parameters is performed manually for a pixel in the centre of the image. Then the entire image is fitted gradually taking the results of the neighboring already fitted pixels as an input for the following one.

At the end $D\nu_a$, $D\nu_b$, $D\nu_c$ and $D\nu_d$, the distance between the two transition for each class of NV centre, are

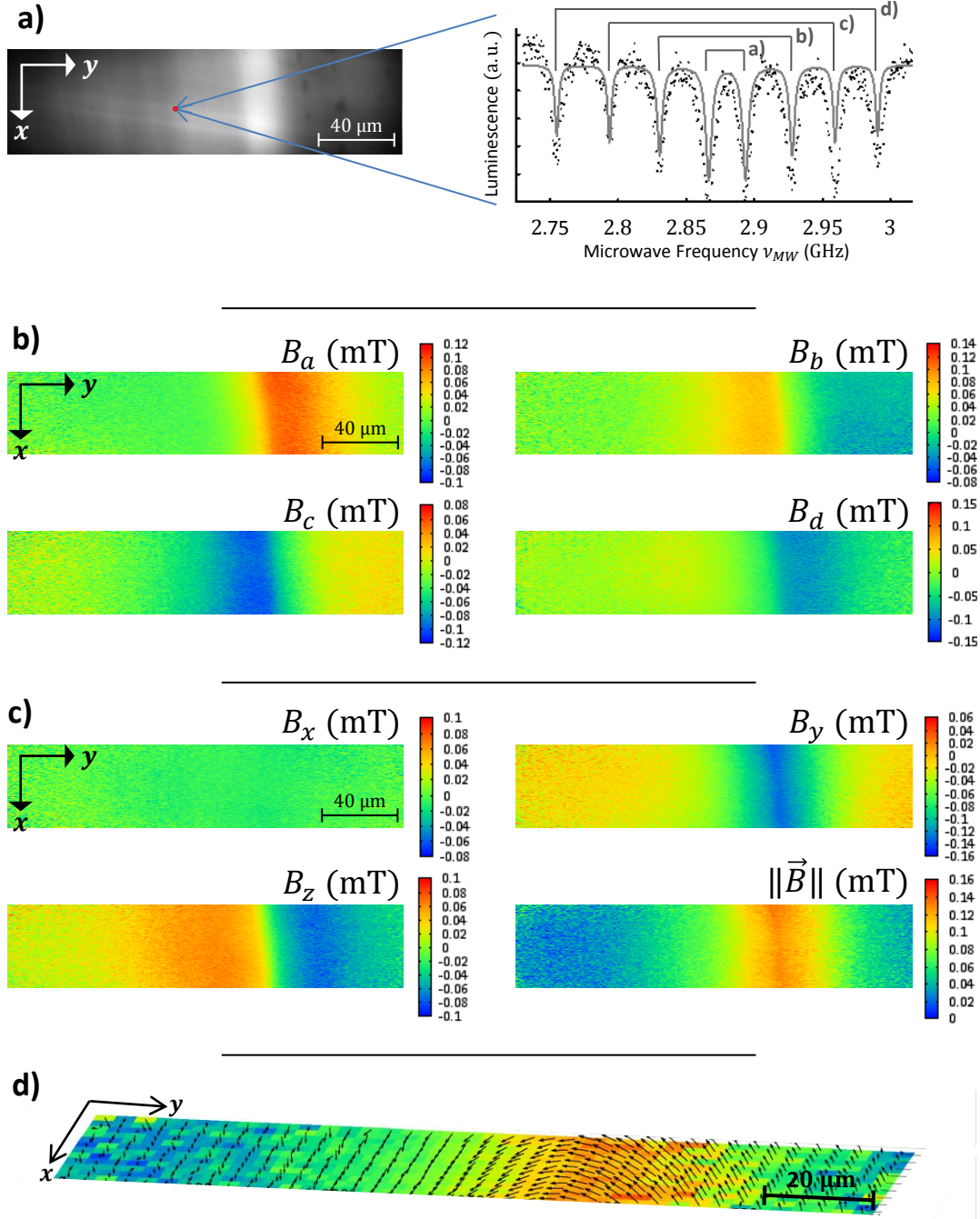


FIG. 3: Illustration of the consecutive steps leading to the vectorial reconstruction a magnetic field with our set-up. The magnetic field is produced by a current of 12 mA within a copper wire located underneath the diamond slab. The field is measured in he plane of the NV⁻ layer. The frequency span is equal to 300 MHz with a sampling of 0.5 MHz. The signal is averaged over 64 sweeps ; **a)** - Image of the luminescence from the NV⁻ centres layer obtained at one given frequency and OMDR spectrum measured for a pixel located at the centre of the image. The raw data are composed of a full OMDR spectrum for each pixel. **b)** - Projection of the magnetic field along the four crystallographic directions (*a*), (*b*), (*c*) and (*d*) for each point in the plane calculated from the raw data by the fitting algorithm ; **c)** - Reconstruction of the magnetic field along each axis (*x*, *y*, *z*) of the laboratory frame (cf. Fig. 2) using the maximum likelihood method and norm of the magnetic field; **d)** - Vectorial representation of the magnetic field produced by the sample in the laboratory frame.

obtained for each pixel of the camera. As a convention, (a), (b), (c) and (d) are chosen in the following order:

$$0 < D\nu_a < D\nu_b < D\nu_c < D\nu_d \quad (4)$$

The measures of the magnetic field B projected on the four possible NV orientations are denoted m_a , m_b , m_c and m_d . Their absolute values are derived using Eq. (2) and Eq. (4). The sign of those projections and the orientation of the axes (a), (b), (c) and (d) with respect to the laboratory frame are then to be determined.

\vec{u}_a , \vec{u}_b , \vec{u}_c and \vec{u}_d are the unit vectors representing the four possible orientations of the NV axes. Due to the symmetry properties of the NV centres, their sum is equal to:

$$\vec{u}_a + \vec{u}_b + \vec{u}_c + \vec{u}_d = \vec{0} \quad (5)$$

so, taking the projection of this equation along the field \vec{B} gives:

$$B_a + B_b + B_c + B_d = 0 \quad (6)$$

Both field \vec{B} and $-\vec{B}$ have exactly the same signature on the NV centres and cannot be distinguished with our system. We choose $B_d > 0$. Then B_b , B_c verifying both Eq. (4) and Eq. (6) have necessarily a sign opposite to that of B_d . In the absence of noise, B_a should be directly deduced from Eq. (6). In the presence of noise, we choose the sign ϵ of B_a , minimizing the relation $\epsilon \cdot D\nu_a - D\nu_b - D\nu_c + D\nu_d$. With this method, we can most probably find the good values of the field projections m_i from the measured $D\nu_i$.

In practice, the fitting algorithm is robust. It returns a reliable value if the contrast C exceeds approximatively twice the noise ratio: $\frac{S}{N} > \frac{2}{C}$ i.e. when the ODMR line is hardly visible from the noise. Considering a typical contrast of 1 % and a signal to noise ratio for a single sweep close to 100 (Table I) an average of only four sweeps is sufficient to successfully retrieve the experimental parameters. The fitting algorithm works with a minimum of 3 or 4 frequency samples within an ODMR line. So considering a typical linewidth of $\Delta\nu = 7$ MHz, a sampling resolution of 2 MHz is sufficient. As a result, for a typical frequency span of $\nu_{span} = 300$ MHz, 150 frequency samples (i.e. images) are necessary. Considering a minimum number of 4 sweeps and an exposure time of 2.5 ms, the minimum duration for the entire measurement is around 1.5 s for a spatial sampling of one pixel on the camera, corresponding to 210 nm on the diamond slab. Instead of accumulating several frequency sweeps, the signal to noise ratio can be increased by spatial binning of the camera pixels. A binning of 5×5 pixels, corresponding to a 1 μm spatial resolution on the diamond slab, requires only one frequency sweep and an acquisition time around 300 ms to result in a signal to noise ratio equivalent to

the one obtained in the previous case. Therefore, an optimization of the spatial resolution / acquisition time can be performed depending on the signal to noise ratio of the ODMR spectrum.

MAGNETIC FIELD RECONSTRUCTION

Once the projections of the magnetic field on the crystallographic axes have been determined, the following step is to reconstruct the magnetic field in the laboratory frame. The measured field components m_i do not directly give the magnetic field B_i , but are affected by some noise inherent to the measurement. To account for that effect, we retrieve the best evaluation of the magnetic field knowing the values of m_i using a maximum-likelihood method.

We define an auxiliary frame which axes are denoted (x_1, y_1, z_1) . Due to the (100) orientation of the diamond, they coincide with the edges of the slab (Fig. 2 a). However, since the orientations of the crystalline axes (a, b, c, d) with respect to the laboratory frame are not known, the auxiliary frame and the laboratory frame do not necessarily coincide. In that frame, \vec{u}_a , \vec{u}_b , \vec{u}_c and \vec{u}_d are chosen with the following coordinates:

$$\begin{aligned} \vec{u}_a &= \frac{1}{\sqrt{3}} \begin{pmatrix} -1 \\ -1 \\ -1 \end{pmatrix}_{(x_1, y_1, z_1)} & \vec{u}_b &= \frac{1}{\sqrt{3}} \begin{pmatrix} 1 \\ 1 \\ -1 \end{pmatrix}_{(x_1, y_1, z_1)} \\ \vec{u}_c &= \frac{1}{\sqrt{3}} \begin{pmatrix} -1 \\ 1 \\ 1 \end{pmatrix}_{(x_1, y_1, z_1)} & \vec{u}_d &= \frac{1}{\sqrt{3}} \begin{pmatrix} 1 \\ -1 \\ 1 \end{pmatrix}_{(x_1, y_1, z_1)} \end{aligned} \quad (7)$$

We consider a Gaussian noise distribution with standard deviation σ . The probability to measure m_a along axis (a) knowing \vec{B} and thus B_a is given by:

$$p(m_a | \vec{B}) \propto e^{-\frac{(B_a - m_a)^2}{2\sigma^2}} \quad (8)$$

Thus, the probability to measure m_a , m_b , m_c and m_d knowing \vec{B} is:

$$p(\{m_i\} | \vec{B}) = \prod_{i=[a,b,c,d]} p(m_i | \vec{B}) \propto \exp(-E) \quad (9)$$

with E given by

$$E = \sum_{i=[a,b,c,d]} \left[\frac{1}{2\sigma^2} (B_i - m_i)^2 \right] \quad (10)$$

According to Bayes theorem, we can interpret Eq. (9) as the likelihood to have a magnetic field equal to \vec{B} , knowing the actual measurements m_a , m_b , m_c and m_d . Thus, the best estimation of \vec{B} would minimize E .

Therefore, we express the projections of the magnetic field on the (i) direction, $B_i = \vec{B} \cdot \vec{u}_i$, as functions of $(B_{x_1}, B_{y_1}, B_{z_1})$ and substitute these expressions in E . Then we minimize E with respect to $(B_{x_1}, B_{y_1}, B_{z_1})$ expressing that its corresponding partial derivatives are zero and obtain the expressions of the most likely magnetic field components as a function of m_a, m_b, m_c and m_d :

$$\begin{aligned} B_{x_1} &= \frac{\sqrt{3}}{4} (-m_a + m_b - m_c + m_d) \\ B_{y_1} &= \frac{\sqrt{3}}{4} (-m_a + m_b + m_c - m_d) \\ B_{z_1} &= \frac{\sqrt{3}}{4} (-m_a - m_b + m_c + m_d) \end{aligned} \quad (11)$$

The advantage of those expressions is to involve the four measured projections of the field, m_i , and, thus, to exploit all the available information. In addition, they are valid even when the sum of the m_i is not strictly equal to zero due to the presence of noise.

At this point there is still an ambiguity on the actual correspondence of axes (x_1, y_1, z_1) with axes (x, y, z) . This can be solved exploiting prior knowledge on the sample. Another possibility is to add an auxiliary known magnetic field (for example by adding a CW current in the antenna), that allows identifying the four lines (a) , (b) , (c) and (d) with respect to the laboratory frame without any prior knowledge on the magnetic field produced by the sample.

As an example, Fig. 3 displays such a reconstruction for a magnetic field produced by a current of 12 mA in a 20 μm diameter copper wire. In this case the shape of the magnetic field distribution that is expected is known a priori which allows to attribute the good directions to the magnetic field components.

SENSITIVITY

In the previous part, we have depicted a method allowing a vectorial reconstruction of the magnetic field starting from the measurement of the field projections on the crystallographic axes. Here, we evaluate the sensitivity of this technique and estimate the maximum sensitivity of our set-up according to our experimental parameters. The minimum detectable magnetic field corresponds to a signal to noise ratio of 1. The measured signal is proportional to the number of photons, N , collected during the integration time. As we showed earlier, the signal is shot-noise limited and affected by Poisson noise. Thus the signal to noise ratio varies as \sqrt{N} and can be improved increasing the number of collected photons. In our set-up, this can be done two ways, first, increasing the number of ODMR spectra that are acquired sequentially and second, increasing the number of pixels and thus the corresponding integration area on the diamond slab active layer. The number of photons is thus proportional to the product of the integration area A and the

integration time T . Therefore, the minimum detectable magnetic field is of the form:

$$\delta B_{min} = \frac{\eta}{\sqrt{TA}} \quad (12)$$

where η is the sensitivity of the set-up that can be derived measuring δB_{min} for various values of T and A .

First, we evaluate the maximal sensitivity that can be expected from our set-up. It is determined from an ODMR line such as the curve (a) of Fig. 4 a). The total luminescence signal is S . The amplitude of the resonance is $S \times C$ where C is the contrast. The linewidth is $\Delta\nu$. The maximum of the slope is obtained close to the line half-maximum and is equal to $\frac{1}{0.77} \cdot \frac{C}{\Delta\nu}$. The factor 0.77 comes from the Lorentzian shape of the line. The noise N is the standard deviation of the monitored signal S .

The sensitivity is calculated from the parameters values obtained for one pixel of the camera that are given in Table I. We obtain [12]:

$$\begin{aligned} \eta_{max} &= \frac{0.77}{g\mu_b/h} \cdot \frac{\Delta\nu}{C \frac{S}{N}} \cdot \sqrt{T \cdot A} \\ &= 2.0 \mu\text{T} \cdot \mu\text{m} / \sqrt{\text{Hz}} \end{aligned} \quad (13)$$

We then determine experimentally the efficiency of the fitting algorithm and compare it with the maximum sensitivity calculated previously. Therefore, we measure two times the same uniform magnetic field consecutively. We then subtract the data and perform a statistics over a large number of 32×32 pixels. The resulting variance is two times the variance of one measurement δB_{fit}^2 . The minimum detectable magnetic field δB_{fit} , normalized to a 1 μm^2 integration area, is given in Fig. 4 b) as a function of the total acquisition time T_{tot} . We have varied either the sampling step or the number of spectrum sweeps. For samplings that are smaller than 2 MHz and for a number of sweeps exceeding 4, the measurement uncertainty decreases as the square root of the total acquisition time. Actually the two ways of increasing the total number of collected photons (increasing the sampling or the number of averaged sweeps) remain totally equivalent (both are plotted indistinctly in Fig. 4 b)). From line 1) in Fig. 4 b), we retrieve the normalized sensitivity of the fitting algorithm:

$$\eta_{fit} = 9.6 \mu\text{T} \cdot \mu\text{m} / \sqrt{\text{Hz}} \quad (14)$$

This value is close, but somewhat higher than η_{max} given by Eq. (13). In fact, in an ODMR spectrum, two lines are necessary to retrieve one magnetic field component and, outside of those two lines, the measurement does not bring any additional information. Therefore, only a fraction $\frac{2\Delta\nu}{\nu_{span}}$ of the total acquisition time T_{tot} is

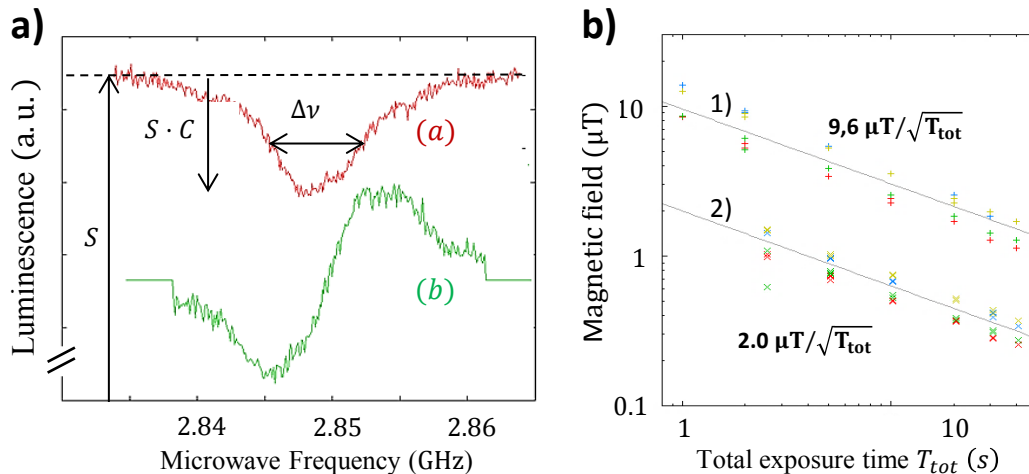


FIG. 4: **a)** - The red curve (a) represents a typical ODMR line. The total luminescence signal is S . The amplitude of the resonance is $S \times C$ where C is the contrast. The linewidth is $\Delta\nu$. The green curve (b) is the error function $Err(\nu)$ obtained by a differential acquisition (Eq. (16)) derived from the ODMR curve (a) ; **b)** - Minimum detectable magnetic field, for a $1 \mu\text{m}^2$ acquisition area, as a function of the total acquisition time. Two cases are represented. The line 1) is obtained with a multi-Lorentzian fitting algorithm. The line 2) is obtained with the differential acquisition method. Those lines allow to retrieve the sensitivities of both methods.

actually useful. The ultimate sensitivity of this method is given by:

$$\eta_{fit} \times \sqrt{\frac{2\Delta\nu}{\nu_{span}}} = 2 \mu\text{T} \cdot \mu\text{m}/\sqrt{\text{Hz}} \quad (15)$$

where only the useful time is considered. This value is similar to the maximal sensitivity value, showing that our fitting algorithm is able to exploit all the useful information available in the ODMR lines.

In order to optimise the measurement time, all the acquisitions have to be taken in the frequency range where the slope of the line is maximum. Having a prior estimation of its position ν , we can acquire two images at frequencies $\nu_a = \nu + \Delta\nu/2$ and $\nu_b = \nu - \Delta\nu/2$. The difference $S(\nu_a) - S(\nu_b)$ is immune from the common mode noise and proportional to the shift of the magnetic field with respect to the central position ν . A normalisation by $S(\nu_a) + S(\nu_b)$ cancels the spatial variation of the pumping beam intensity. We can then calculate the error function

$$Err(\nu) = \frac{S(\nu_a) - S(\nu_b)}{S(\nu_a) + S(\nu_b)} \quad (16)$$

that is represented by the curve (b) of Fig. 4 a). Knowing the contrast and the linewidth, we can retrieve the minimum detectable magnetic field from the measured signal as a function of the total acquisition time T_{tot} . It is fitted by the line 2) in Fig. 4 b). The resulting sensitivity is

$$\eta_{diff} = 2.0 \mu\text{T} \cdot \mu\text{m}/\sqrt{\text{Hz}} \quad (17)$$

which matches exactly the value of η_{max} . Therefore this differential method allows to obtain the maximum sensitivity of our set-up once the line positions have been

determined by the fitting algorithm. Another advantage of this differential method is that the measurement of the slope requires only two frequency measurements and thus two images, leading to potentially much shorter acquisition times.

CONCLUSION

In this work, we have exploited the ODMR signal of an ensemble of NV centers in order to quantitatively map the vectorial structure of a magnetic field produced by a sample close to the surface of a CVD diamond hosting a thin layer of NV centers. The reconstruction of the magnetic field is based on a maximum-likelihood technique which exploits the response of the four intrinsic orientations of the NV center inside the diamond lattice. The sensitivity associated to a $1 \mu\text{m}^2$ area of the doped layer, equivalent to a sensor consisting of approximately 10^4 NV centers, is of the order of $2 \mu\text{T}/\sqrt{\text{Hz}}$. The spatial resolution of the imaging device is 400 nm, limited by the numerical aperture of the optical microscope which is used to collect the photoluminescence of the NV layer. The versatility of the sensor is illustrated by the accurate reconstruction of the magnetic field created by a DC current inside a copper wire deposited on the diamond sample.

Several improvements can be considered to increase the sensitivity of the device. Using a camera with a higher dynamics would allow to increase the maximum number of photons per pixel before saturation, and thus increase the signal to noise ratio. The CW pumping of our device

may induce power broadening of the OMDR line [21]. Pumping in pulsed regime may avoid this limitation. The sample can also be improved. Increasing the yield of the N to NV conversion [28] would allow to decrease the number of residual Nitrogen atoms surrounding the NV⁻ centers. This may avoid a possible broadening of the OMDR linewidth due to the nuclear spin bath.

ACKNOWLEDGEMENTS

The research leading to these results has received funding from the European Union Seventh Framework Programme (FP7/2007-2013) under the project DIADEMS (grant agreement n° 611143) and from the Agence Nationale de la Recherche (ANR) under the project ADVICE (grant ANR-2011-BS04-021).

* Electronic address: thierry.debuisschert@thalesgroup.com

- [1] Robert McDermott, SeungKyun Lee, Bennie ten Haken, Andreas H. Trabesinger, Alexander Pines, and John Clarke. Microtesla mri with a superconducting quantum interference device. *Proceedings of the National Academy of Sciences of the United States of America*, 101(21):7857–7861, 2004.
- [2] D. Rugar, R. Budakian, H. J. Mamin, and B. W. Chui. Single spin detection by magnetic resonance force microscopy. *Nature*, 430(6997):329–332, July 2004.
- [3] C. L. Degen, M. Poggio, H. J. Mamin, C. T. Rettner, and D. Rugar. Nanoscale magnetic resonance imaging. *Proceedings of the National Academy of Sciences*, 106(5):1313–1317, 2009.
- [4] M. P. Ledbetter, I. M. Savukov, D. Budker, V. Shah, S. Knappe, J. Kitching, D. J. Michalak, S. Xu, and A. Pines. Zero-field remote detection of nmr with a microfabricated atomic magnetometer. *Proceedings of the National Academy of Sciences*, 105(7):2286–2290, 2008.
- [5] Shoujun Xu, Valeriy V. Yashchuk, Marcus H. Donaldson, Simon M. Rochester, Dmitry Budker, and Alexander Pines. Magnetic resonance imaging with an optical atomic magnetometer. *Proceedings of the National Academy of Sciences*, 103(34):12668–12671, 2006.
- [6] A. Gruber, A. Dräbenstedt, C. Tietz, L. Fleury, J. Wrachtrup, and C. Von Borczyskowski. Scanning confocal optical microscopy and magnetic resonance on single defect centers. *Science*, 276(5321):2012–2014, June 1997.
- [7] N. Manson, J. Harrison, and M. Sellars. Nitrogen-vacancy center in diamond: Model of the electronic structure and associated dynamics. *Phys. Rev. B*, 74(10), September 2006.
- [8] Gopalakrishnan Balasubramanian, Philipp Neumann, Daniel Twitchen, Matthew Markham, Roman Kolesov, Norikazu Mizuochi, Junichi Isoya, Jocelyn Achard, Johannes Beck, Julia Tisler, Vincent Jacques, Philip R. Hemmer, Fedor Jelezko, and Jörg Wrachtrup. Ultralong spin coherence time in isotopically engineered diamond. *Nat. Mat.*, 8(5):383–387, April 2009.
- [9] Nir Bar-Gill, Linh M Pham, Andrejs Jarmola, Dmitry Budker, and Ronald L Walsworth. Solid-state electronic spin coherence time approaching one second. *Nature communications*, 4:1743, 2013.
- [10] Toyofumi Ishikawa, Kai-Mei C. Fu, Charles Santori, Victor M. Acosta, Raymond G. Beausoleil, Hideyuki Watanabe, Shinichi Shikata, and Kohei M. Itoh. Optical and spin coherence properties of nitrogen-vacancy centers placed in a 100 nm thick isotopically purified diamond layer. *Nano Letters*, 12(4):2083–2087, 2012.
- [11] J-P Tetteien, L Rondin, P Spinicelli, M Chipaux, T Debuisschert, J-F Roch, and V Jacques. Magnetic-field-dependent photodynamics of single nv defects in diamond: an application to qualitative all-optical magnetic imaging. *New Journal of Physics*, 14(10):103033, 2012.
- [12] J. M. Taylor, P. Cappellaro, L. Childress, L. Jiang, D. Budker, P. R. Hemmer, A. Yacoby, R. Walsworth, and M. D. Lukin. High-sensitivity diamond magnetometer with nanoscale resolution. *Nat. Phys*, 4(10):810–816, September 2008.
- [13] Chi-Cheng Fu, Hsu-Yang Lee, Kowa Chen, Tsong-Shin Lim, Hsiao-Yun Wu, Po-Keng Lin, Pei-Kuen Wei, Pei-Hsi Tsao, Huan-Cheng Chang, and Wunshain Fann. Characterization and application of single fluorescent nanodiamonds as cellular biomarkers. *Proceedings of the National Academy of Sciences*, 104(3):727–732, 2007.
- [14] Gopalakrishnan Balasubramanian, I. Y. Chan, Roman Kolesov, Mohannad Al-Hmoud, Julia Tisler, Chang Shin, Changdong Kim, Aleksander Wojcik, Philip R. Hemmer, Anke Krueger, Tobias Hanke, Alfred Leitenstorfer, Rudolf Bratschitsch, Fedor Jelezko, and Jörg Wrachtrup. Nanoscale imaging magnetometry with diamond spins under ambient conditions. *Nature*, 455(7213):648–651, October 2008.
- [15] J. R. Maze, P. L. Stanwix, J. S. Hodges, S. Hong, J. M. Taylor, P. Cappellaro, L. Jiang, M. V. Gurudev Dutt, E. Togan, A. S. Zibrov, A. Yacoby, R. L. Walsworth, and M. D. Lukin. Nanoscale magnetic sensing with an individual electronic spin in diamond. *Nature*, 455(7213):644–647, October 2008.
- [16] M. V. Gurudev Dutt, L. Childress, L. Jiang, E. Togan, J. Maze, F. Jelezko, A. S. Zibrov, P. R. Hemmer, and M. D. Lukin. Quantum register based on individual electronic and nuclear spin qubits in diamond. *Science*, 316(5829):1312–1316, 2007.
- [17] Philipp Neumann, Johannes Beck, Matthias Steiner, Florian Rempp, Helmut Fedder, Philip R. Hemmer, Jrg Wrachtrup, and Fedor Jelezko. Single-shot readout of a single nuclear spin. *Science*, 329(5991):542–544, 2010.
- [18] P. Neumann, R. Kolesov, B. Naydenov, J. Beck, F. Rempp, M. Steiner, V. Jacques, G. Balasubramanian, M. L. Markham, D. J. Twitchen, S. Pezzagna, J. Meijer, J. Twamley, F. Jelezko, and J. Wrachtrup. Quantum register based on coupled electron spins in a room-temperature solid. *Nat Phys*, 6(4):249–253, April 2010.
- [19] P. Maletinsky, S. Hong, M. S. Grinolds, B. Hausmann, M. D. Lukin, R. L. Walsworth, M. Loncar, and A. Yacoby. A robust scanning diamond sensor for nanoscale imaging with single nitrogen-vacancy centres. *Nat. Nano.*, 7(5):320–324, April 2012.
- [20] MS Grinolds, S Hong, P Maletinsky, L Luan, MD Lukin, RL Walsworth, and A Yacoby. Nanoscale magnetic imaging of a single electron spin under ambient conditions. *Nature Physics*, 9(4):215–219, 2013.

- [21] A. Dréau, M. Lesik, L. Rondin, P. Spinicelli, O. Arcizet, J.-F. Roch, and V. Jacques. Avoiding power broadening in optically detected magnetic resonance of single NV defects for enhanced dc magnetic field sensitivity. *Phys. Rev. B*, 84(19):195204, November 2011.
- [22] L. Rondin, J.-P. Tetienne, P. Spinicelli, C. Dal Savio, K. Karrai, G. Dantelle, A. Thiaville, S. Rohart, J.-F. Roch, and V. Jacques. Nanoscale magnetic field mapping with a single spin scanning probe magnetometer. *Appl. Phys. Lett.*, 100(15):–, 2012.
- [23] J.-P. Tetienne, T. Hingant, J.-V. Kim, L. Herrera Diez, J.-P. Adam, K. Garcia, J.-F. Roch, S. Rohart, A. Thiaville, D. Ravelosona, and V. Jacques. Nanoscale imaging and control of domain-wall hopping with a nitrogen-vacancy center microscope. *Science*, 344(6190):1366–1369, 2014.
- [24] S. Steinert, F. Dolde, P. Neumann, A. Aird, B. Naydenov, G. Balasubramanian, F. Jelezko, and J. Wrachtrup. High sensitivity magnetic imaging using an array of spins in diamond. *Rev. Sci. Instrum.*, 81(4):043705–043705–5, April 2010.
- [25] L M Pham, D Le Sage, P L Stanwix, T K Yeung, D Glenn, A Trifonov, P Cappellaro, P R Hemmer, M D Lukin, H Park, A Yacoby, and R L Walsworth. Magnetic field imaging with nitrogen-vacancy ensembles. *New J. Phys.*, 13(4):045021, April 2011.
- [26] D Le Sage, K Arai, DR Glenn, SJ DeVience, LM Pham, L Rahn-Lee, MD Lukin, A Yacoby, A Komeili, and RL Walsworth. Optical magnetic imaging of living cells. *Nature*, 496(7446):486–489, 2013.
- [27] A. Tallaire, A.T. Collins, D. Charles, J. Achard, R. Sussmann, A. Gicquel, M.E. Newton, A.M. Edmonds, and R.J. Cruddace. Characterisation of high-quality thick single-crystal diamond grown by CVD with a low nitrogen addition. *Diam. Rel. Mat.*, 15(10):1700–1707, October 2006.
- [28] S Pezzagna, B Naydenov, F Jelezko, J Wrachtrup, and J Meijer. Creation efficiency of nitrogen-vacancy centres in diamond. *New Journal of Physics*, 12(6):065017, 2010.
- [29] Kenneth Levenberg. A method for the solution of certain problems in least squares. *Quarterly of applied mathematics*, 2:164–168, 1944.
- [30] Donald W Marquardt. An algorithm for least-squares estimation of nonlinear parameters. *Journal of the Society for Industrial & Applied Mathematics*, 11(2):431–441, 1963.